Systematic analysis of reaction cross sections of carbon isotopes

W. Horiuchi,[1] Y. Suzuki,[2] B. Abu-Ibrahim,[3,4] and A. Kohama[3]
[1]*Graduate School of Science and Technology, Niigata University, Niigata 950-2181, Japan*
[2]*Department of Physics and Graduate School of Science and Technology, Niigata University, Niigata 950-2181, Japan*
[3]*RIKEN Nishina Center, Wako-shi, Saitama 351-0198, Japan*
[4]*Department of Physics, Cairo University, Giza 12613, Egypt*
(Received 10 December 2006; published 20 April 2007)

We systematically analyze total reaction cross sections of carbon isotopes with $N = 6$–16 on a ^{12}C target for wide range of incident energy. The intrinsic structure of the carbon isotope is described by a Slater determinant generated from a phenomenological mean-field potential, which reasonably well reproduces the ground-state properties for most of the even N isotopes. We need separate studies not only for odd nuclei but also for ^{16}C and ^{22}C to improve their wave functions. The density of the carbon isotope is constructed by eliminating the effect of the center-of-mass motion. For the calculations of the cross sections, we take two schemes, the Glauber approximation and the eikonal model using a global optical potential. Both the reaction models successfully reproduce low and high incident energy data on the cross sections of ^{12}C, ^{13}C, and ^{16}C on ^{12}C. The calculated reaction cross sections of ^{15}C are found to be considerably smaller than the empirical values observed at low energy. We find a consistent parametrization of the nucleon-nucleon scattering amplitude, differently from previous ones. Finally, we predict the total reaction cross section of ^{22}C on ^{12}C.

DOI: 10.1103/PhysRevC.75.044607 PACS number(s): 25.60.Dz, 21.10.Gv, 24.10.−i, 25.70.−z

I. INTRODUCTION

The structure of carbon isotopes has recently attracted much attention as experimental information accumulated toward its neutron dripline. The topics discussed include, for example, the subshell closure of $N = 14$ and $N = 16$ and the anomalously small $E2$ transition strength observed in ^{16}C [1,2]. These issues are closely related to the competition of $0d_{5/2}$ and $1s_{1/2}$ neutron orbits. In fact, they play a predominant role in determining the ground-state structure of the carbon isotope with $N > 8$.

The momentum distribution of a ^{15}C fragment in the breakup of ^{16}C suggests that the last neutrons in ^{16}C occupy both the $0d_{5/2}$ and $1s_{1/2}$ orbits [3], which is consistent with recent ^{14}C+n+n three-body calculations [4,5]. The $1s_{1/2}$ orbit plays a vital role in forming a one-neutron halo structure of ^{19}C [6,7]. If the subshell closure of $N = 14$ is a good approximation in the carbon isotopes, the $0d_{5/2}$ orbits are fully occupied in the nucleus ^{20}C. Adding one more neutron to ^{20}C leads to no particle-bound system, but ^{22}C, getting one more neutron, becomes bound. ^{22}C is thus a Borromean nucleus. The structure of ^{22}C has recently been studied by two (W.H. and Y.S.) of the present authors in the three-body model of $^{20}\mathrm{C} + n + n$ [8].

A molecular picture in ^{14}C is investigated in the framework of three α particles plus two neutrons [9]. The deformation of the carbon isotopes is also discussed to have a strong N dependence [10,11]. The properties of the carbon isotopes are reviewed in Ref. [12] based on the mean-field and shell-model configuration mixing models.

How do such nuclear structures affect reaction data? Nowadays, the data on total reaction or interaction cross sections have accumulated particularly for light nuclei. In the case of the carbon isotopes, for example, the interaction cross section has been measured up to ^{20}C around 700∼960A MeV incident energy [13]. Because these cross sections reflect the size of nuclei, it is interesting to analyze the cross sections in a systematic manner.

The purpose of the present study is a systematic analysis of the total reaction cross sections of carbon isotopes on a ^{12}C target using two reaction models which enable us to go beyond a folding model; the Glauber model [14] and the eikonal approximation [15,16] with the use of nucleon-^{12}C optical potentials. This study is also motivated by an ongoing measurement of the reaction cross section of ^{22}C [17]. Such a measurement looks quite challenging because the production rate of ^{22}C is expected to be small. We will perform a simple, consistent, *ad hoc* parameter-free analysis. The systematics will offer an interesting interplay between nuclear structure models and the reaction models.

The input parameters on nucleon-nucleon scatterings needed in the Glauber calculation is carefully assessed using available ^{12}C+^{12}C reaction cross-section data. The wave function of a carbon isotope is first generated from a Slater determinant whose nucleon orbits are built from phenomenological mean-field potentials, and the corresponding neutron and proton densities, with its center-of-mass (c.m.) motion being taken into account properly, are constructed for the calculation of the total reaction cross section. The asymptotic form of the wave function is carefully described by the use of empirical nucleon separation energies as it is important for the cross section calculation, particularly for a spatially extended system. A comparison with experimental cross sections will immediately reveal a successful or unsuccessful case. To resolve the discrepancy between theory and experiment, one has to go beyond the simple mean-field model and two types of dynamical models are performed to obtain an improved density. One is a core+n model for an odd N nucleus, and the other is a core+n+n model for ^{16}C and ^{22}C.

The organization of the present article is as follows: The reaction models for a calculation of reaction cross sections

between nuclei are presented in the next section. A simple formula is given in Sec. II A in the framework of the Glauber theory, and the other method using an optical potential is explained in Sec. II B. The reaction cross section of ^{12}C+^{12}C is tested by these formulas in a wide range of incident energy. In Sec. III the phenomenological mean-field potential is prescribed for generating the Slater determinant, and the c.m. motion is removed to obtain the intrinsic density that is used in the reaction calculation. The mean radius of the matter distribution is compared to the empirical value. The nuclear structure model is extended to the dynamical model in Sec. IV. A core+n model is applied to the odd N isotopes in Sec. IV A, where the difference in the densities between the dynamical model and the Slater determinant is discussed. The binding energy and the matter size of ^{22}C are studied in the three-body model of ^{20}C+n+n in Sect. IV B and the densities of the core+n+n model are presented in Sec. IV C. Section V presents the results of reaction cross section calculations; the cases of $^{12-20}$C in Sec. V A and the ^{22}C+^{12}C reaction in Sec. V B. Summary is drawn in Sec. VI. A method of calculation of two-particle distribution functions is given in Appendix.

II. MODEL FOR A REACTION CROSS-SECTION CALCULATION

In this section, we describe our reaction models for analyzing reaction cross sections between nuclei. A simple formula is given in Sec. II A in the framework of the Glauber theory, and the other method using an optical potential is explained in Sec. II B. These methods are complementary to each other for a ^{12}C target, but only the former can be applied for a proton target in general when a proton-nucleus optical potential is not available. With these calculations in two ways, we can find a reliable parametrization of the NN interaction for a wide energy range, which is important to proceed to the case of a proton target in our future work.

A. Glauber formalism

The reaction cross section for a projectile-target collision is calculated by integrating the reaction probability with respect to the impact parameter $\boldsymbol{b}$;

$$\sigma_{\rm R} = \int d\boldsymbol{b}(1 - |e^{i\chi(\boldsymbol{b})}|^2), \tag{1}$$

where the phase-shift function χ is expressed, in the Glauber model [14], through the NN profile function Γ_{NN} by

$$e^{i\chi(\boldsymbol{b})} = \langle \Psi_0\Theta_0|\prod_{i\in {\rm P}}\prod_{j\in {\rm T}}[1 - \Gamma_{NN}(\boldsymbol{s}_i - \boldsymbol{t}_j + \boldsymbol{b})]|\Psi_0\Theta_0\rangle. \tag{2}$$

Here Ψ_0 (Θ_0) is the intrinsic wave function of the projectile (target) with its c.m. part being removed, $\boldsymbol{s}_i$ is the two-dimensional vector of the projectile's single-particle coordinate, $\boldsymbol{r}_i$, measured from the projectile's c.m. coordinate, and $\boldsymbol{t}_i$ is defined for the target nucleus in a similar way. The profile function Γ_{NN} is usually parameterized in the form;

$$\Gamma_{NN}(\boldsymbol{b}) = \frac{1 - i\alpha}{4\pi\beta}\sigma_{NN}^{\rm tot}\exp\left(-\frac{\boldsymbol{b}^2}{2\beta}\right), \tag{3}$$

where $\sigma_{NN}^{\rm tot}$ is the total cross section for NN collisions, α the ratio of the real to the imaginary part of the NN scattering amplitude, and β the slope parameter of the NN elastic differential cross section.

As seen in Eq. (2), the calculation of the phase-shift function requires a multidimensional integration. The importance of including such higher-order terms has been known for many years [18]. Though the integration can be performed using the Monte Carlo technique even for sophisticated wave functions [19], it is fairly involved in general, so it is often approximately evaluated in the optical limit approximation (OLA) using the intrinsic densities of the projectile (target) nuclei, $\rho_{\rm P}$ ($\rho_{\rm T}$), as follows:

$$e^{i\chi_{\rm OLA}(\boldsymbol{b})} = \exp\left[-\iint d\boldsymbol{r}d\boldsymbol{r}'\rho_{\rm P}(\boldsymbol{r})\rho_{\rm T}(\boldsymbol{r}')\Gamma_{NN}(\boldsymbol{s} - \boldsymbol{t} + \boldsymbol{b})\right]. \tag{4}$$

Another approximation is proposed in Ref. [20] by two (B.A.-I. and Y.S.) of the present authors to calculate the reaction cross sections using the same input as in the OLA. The essence of the approximation is to consider, as an intermediate step, a phase shift function for the nucleon-nucleus scattering. With the introduction of the profile function Γ_{NT} for the nucleon-target (NT) scattering, the phase-shift function of OLA, Eq. (4), is replaced by $\bar{\chi}$ as

$$\begin{aligned} e^{i\bar{\chi}(\boldsymbol{b})} &= \langle\Psi_0|\prod_{i\in {\rm P}}\{1 - \Gamma_{NT}(\boldsymbol{s}_i + \boldsymbol{b})\}|\Psi_0\rangle \\ &\approx \exp\left[-\int d\boldsymbol{r}\rho_{\rm P}(\boldsymbol{r})\Gamma_{NT}(\boldsymbol{s} + \boldsymbol{b})\right]. \end{aligned} \tag{5}$$

We here adopt two methods to calculate the Γ_{NT}: One is to calculate the Γ_{NT} using an appropriate optical potential as shown in the next subsection. The other is to use the Glauber theory as

$$\begin{aligned} \Gamma_{NT}(\boldsymbol{b}) &= 1 - \langle\Theta_0|\prod_{j\in {\rm T}}[1 - \Gamma_{NN}(\boldsymbol{b} - \boldsymbol{t}_j)]|\Theta_0\rangle \\ &\approx 1 - \exp\left[-\int d\boldsymbol{r}'\rho_{\rm T}(\boldsymbol{r}')\Gamma_{NN}(\boldsymbol{b} - \boldsymbol{t})\right]. \end{aligned} \tag{6}$$

Substituting this expression into Eq. (5) leads us to

$$\begin{aligned} e^{i\bar{\chi}(\boldsymbol{b})} &= \exp\Bigg(-\int d\boldsymbol{r}\rho_{\rm P}(\boldsymbol{r}) \\ &\quad\times\left\{1 - \exp\left[-\int d\boldsymbol{r}'\rho_{\rm T}(\boldsymbol{r}')\Gamma_{NN}(\boldsymbol{s} - \boldsymbol{t} + \boldsymbol{b})\right]\right\}\Bigg). \end{aligned} \tag{7}$$

This formula is found to give better results than those of the OLA [20,21]. Though only the leading term in the cumulant expansion is taken into account to derive Eq. (7), this approximation includes higher-order corrections which Eq. (4) does not contain [21]. Because the role of the projectile and the target is interchangeable in the calculation of the reaction cross

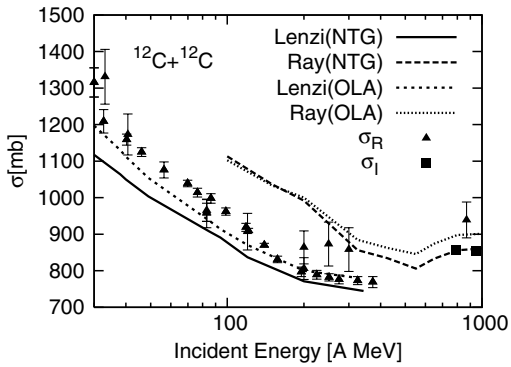

FIG. 1. Reaction cross sections of ^{12}C on a ^{12}C target calculated with the parameters of Refs. [22,23]. The experimental data are taken from Refs. [24–31] for the reaction cross section σ_R and from Ref. [13] for the interaction cross section σ_I.

section, it may be possible to symmetrize Eq. (7) as follows:

$$e^{i\tilde{\chi}(\boldsymbol{b})} = \exp\left(-\frac{1}{2}\int d\boldsymbol{r}\rho_P(\boldsymbol{r}) \times\left\{1-\exp\left[-\int d\boldsymbol{r}'\rho_T(\boldsymbol{r}')\Gamma_{NN}(\boldsymbol{s}-\boldsymbol{t}+\boldsymbol{b})\right]\right\}\right) \times\exp\left(-\frac{1}{2}\int d\boldsymbol{r}'\rho_T(\boldsymbol{r}') \times\left\{1-\exp\left[-\int d\boldsymbol{r}\rho_P(\boldsymbol{r})\Gamma_{NN}(\boldsymbol{t}-\boldsymbol{s}+\boldsymbol{b})\right]\right\}\right). \quad (8)$$

This approximation is called NTG hereafter, which stands for the NT profile function in the Glauber model.

The parameters of Γ_{NN} are taken from Refs. [22,23]. In the latter case [23] the parameters are given for the *pp* and *pn* collisions separately, but here we use the mean values because the target nucleus is ^{12}C whose proton and neutron densities are virtually the same to good accuracy. In Fig. 1 we compare the numerical results obtained using these parameters with the experimental data of ^{12}C+^{12}C total reaction cross sections. Here the intrinsic density of ^{12}C is obtained from the procedure that will be explained in the next section. It is found that both the parameters give quite different cross sections at 100∼300A MeV. Apparently the cross sections obtained with the parameters of Ref. [23] are too large, whereas those with the parameters of Ref. [22] tend to be a little smaller than experiment.

The *NN* profile function could be subject to change from that of the free space especially at lower energies because of the effects due to the Pauli blocking and the Fermi motion of the nucleons [32]. Warner *et al*. studied the in-medium effect on the reaction cross section by modifying the free $\sigma_{NN}^{\rm tot}$ [33]. Takechi *et al*. have recently reported that taking into account the Fermi motion leads to a significant change in the $\sigma_{NN}^{\rm tot}$ values, which is vital to reproduce the reaction cross sections at lower energies [34].

Here we take a simpler route: First, we note that the total elastic cross section $\sigma_{NN}^{\rm el}$ of the *NN* collision is given by

$$\sigma_{NN}^{\rm el} = \frac{1+\alpha^2}{16\pi\beta}\left(\sigma_{NN}^{\rm tot}\right)^2 \quad (9)$$

for the profile function of Eq. (3) [35]. Then, for $E<300A$ MeV where only the elastic scattering is energetically possible as the pion production threshold is closed, we expect that the relation of $\sigma_{NN}^{\rm el}=\sigma_{NN}^{\rm tot}$ should hold from the unitarity of the *NN* collision. Employing the parameters of Ref. [23] yields $\sigma_{NN}^{\rm el}=17$, 7, and 3 mb at $E=100$, 150, and 200 MeV, respectively, which are far smaller than the $\sigma_{NN}^{\rm tot}$ values at the corresponding energies. We, instead, choose the β value for $E<300A$ MeV as

$$\beta = \frac{1+\alpha^2}{16\pi}\sigma_{NN}^{\rm tot} \quad (10)$$

to satisfy the equality of $\sigma_{NN}^{\rm el}=\sigma_{NN}^{\rm tot}$. For $E>300A$ MeV where the equality breaks down, the β values are determined from Eq. (9) using the experimental values of $\sigma_{NN}^{\rm el}=\frac{1}{2}(\sigma_{pp}^{\rm el}+\sigma_{pn}^{\rm el})$ [36]. Some of the α parameters of Ref. [22] are also modified to follow the systematics of Ref. [23].

Table I lists the parameters of the *NN* profile function used in the present study. The ^{12}C+^{12}C reaction cross sections calculated using these parameters are displayed by solid (NTG) and dotted (OLA) lines in Fig. 2. We find that the modified parameter set reproduces very well the experiment in the whole energy region. The NTG phase shift function is found to reproduce the cross section better than the OLA. We thus conclude that both the calculated density of ^{12}C and the parameter set of Γ_{NN} are qualified for a systematic analysis of the reaction cross section of the carbon isotopes on a ^{12}C target.

B. Nucleon-nucleus data as a basic input

In this subsection, we briefly present a method developed in Refs. [14,20] for describing nucleus-nucleus scattering using an optical potential for the nucleon-nucleus elastic scattering.

TABLE I. Parameters of the *NN* profile function. E is the projectile's incident energy. Some parameters are modified from the original values of Refs. [22,23]. See the text for detail.

E (A MeV)	$\sigma_{NN}^{\rm tot}$ (fm^2)	α	β (fm^2)
30	19.6	0.87	0.685
38	14.6	0.89	0.521
40	13.5	0.9	0.486
49	10.4	0.94	0.390
85	6.1	1.37	0.349
94	5.5	1.409	0.327
100	5.295	1.435	0.322
120	4.5	1.359	0.255
150	3.845	1.245	0.195
200	3.45	0.953	0.131
325	3.03	0.305	0.075
425	3.03	0.36	0.078
550	3.62	0.04	0.125
650	4.0	−0.095	0.16
800	4.26	−0.07	0.21
1000	4.32	−0.275	0.21

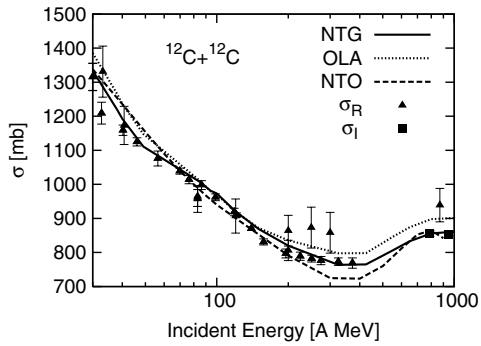

FIG. 2. Comparison of the reaction cross sections of ^{12}C on a ^{12}C target between theory and experiment. The input parameters for Γ_{NN} are taken from Table I in the NTG and OLA calculations, while those for Γ_{NT} are taken from the global optical potential of Ref. [37] in the NTO calculation. At energies less than 100A MeV the correction due to the deviation from the straight-line trajectory, though negligibly small, is included in the NTO calculation. See the caption of Fig. 1 for the experimental data.

Denoting the NT optical potential by V_{NT}, we define the corresponding phase shift function χ_{NT} as

$$\chi_{NT}(\boldsymbol{b}) = -\frac{1}{\hbar v}\int_{-\infty}^{\infty} dz V_{NT}(\boldsymbol{b} + z\hat{\boldsymbol{z}}), \tag{11}$$

where v is the incident velocity of the NT relative motion. Now we express the NT profile function as

$$\Gamma_{NT}(\boldsymbol{b}) = 1 - \mathrm{e}^{i\chi_{NT}(\boldsymbol{b})}. \tag{12}$$

The substitution of Eq. (12) into Eq. (5) yields another formula to calculate the optical phase shift function. We call this approximation NTO, which stands for the NT formalism with the optical potential. Similarly to NTG, the reaction cross section given by NTO includes higher-order terms that are missing in the reaction cross section calculated with a folding model. In the latter model the phase shift function χ_f is simply given by

$$\mathrm{e}^{i\chi_f(\boldsymbol{b})} = \exp\left[i\int d\boldsymbol{r}\rho_{\mathrm{P}}(\boldsymbol{r})\chi_{NT}(\boldsymbol{b}+\boldsymbol{s})\right]. \tag{13}$$

The needed input for NTO is the projectile's intrinsic density and the optical potential V_{NT} at a given energy. As V_{NT} we use the central part of the global optical potential EDAD-fit3 (GOP) [37], which is determined by a Dirac phenomenology. This potential, together with the other EDAD sets, gives a good fit to p+^{12}C elastic scattering and reaction cross-section data in the incident energy of 30 MeV to 1 GeV. It should be noted, however, that the EDAD-fit3 potential predicts slightly smaller reaction cross sections than experiment in the intermediate energy range of 300–400 MeV. This would be due to the lack of data of p+^{12}C elastic scattering differential cross section for this energy range. We ignore the difference between pT and nT interactions in this study.

The NTO calculation for ^{12}C+^{12}C reaction cross section is shown by dashed line in Fig. 2. As we see, the agreement between experiment and theory is good. The underestimation of the cross section around 300–400A MeV is probably due to the smaller absorption of the EDAD-fit3 potential as noted above. An advantage of these calculations is that they are parameter free. For the energy less than 300A MeV, the numerical results with NTO as well as with NTG agree with the data quite well.

At energies less than 100A MeV, the correction due to the deviation from the straight-line trajectory was studied for ^{12}C+^{12}C case. We used the distance of the closest approach in Rutherford orbit in place of the asymptotic impact parameter [38]. This correction is found to be small. It decreases the reaction cross section by only few percentages at 30A MeV.

For high-energy side, we note that the reaction cross section calculated using NTO slightly decreases at 900A MeV. This is due to the fact that the imaginary part of the GOP reaches its deepest value at 800A MeV and then decreases by a small amount as the energy increases.

Our results underestimate the data of the total reaction cross sections at 870A MeV [31]. The numerical results unexpectedly agree with the data of the interaction cross sections at 790 and 950A MeV [13], but not with the total reaction cross section. Because our result is quite close to the one ($\sigma_{\mathrm{R}} = 865 \pm 1$ mb) obtained from a more sophisticated calculation [19], the approximation that we used must be in appropriate direction. Possible uncertainties comes from the parameters of NN scattering amplitude and/or the data of σ_{R} itself. To clarify the situation, a more accurate measurement of such quantities at high energy will be useful.

If we believe the data of σ_{R} at 870A MeV, we need a steep increase of the cross section from 400A MeV toward higher energies to reproduce it while the energy dependence of our results is rather weak. As one can see from Fig. 1, compared with OLA, the NTG, which resums higher-order corrections coming from the first cumulant as in Eq. (8), reduces the magnitude of the cross section for the region of the energy higher than 200A MeV, and causes a weak energy dependence for this energy region.

In contrast to our results, a rather strong energy dependence is obtained by Iida *et al*. based on the black-sphere picture of nuclei [39]. These authors reproduce the total reaction cross section at 870A MeV [31] as well as the data between 100 and 400A MeV due to the steep increase of the cross section. However, they failed to reproduce the energy dependence of low energy side, because their picture breaks down for low energy, less than around 100A MeV.

Other works, for example, Refs. [28,33], deal with ^{12}C+^{12}C reactions of wide range of incident energy and reproduce the reaction cross section at 870A MeV. However, in the energy of 100–400A MeV, their results agree with the old data [28], the larger ones, not the recent smaller ones [24]. Therefore, these theoretical results overestimate the cross sections in this energy region, and the weak energy dependence of their results leads to reproducing the reaction cross section at 870A MeV.

III. DENSITY WITH A SLATER DETERMINANT

Now we discuss the densities of the carbon isotopes, which will be applied to the calculation of total reaction cross sections.

TABLE II. Neutron configurations for the ground states of the carbon isotopes. J^π is the spin-parity of the ground state.

Nucleus	J^π	Configurations
^{12}C	0^+	$(0s_{1/2})^2(0p_{3/2})^4$
^{13}C	$\frac{1}{2}^-$	$(0s_{1/2})^2(0p_{3/2})^4(0p_{1/2})^1$
^{14}C	0^+	$(0s_{1/2})^2(0p_{3/2})^4(0p_{1/2})^2$
^{15}C	$\frac{1}{2}^+$	$(0s_{1/2})^2(0p_{3/2})^4(0p_{1/2})^2(1s_{1/2})^1$
^{16}C	0^+	$(0s_{1/2})^2(0p_{3/2})^4(0p_{1/2})^2(0d_{5/2})^2$
^{17}C	—	$(0s_{1/2})^2(0p_{3/2})^4(0p_{1/2})^2(0d_{5/2})^2(1s_{1/2})^1$
	—	$(0s_{1/2})^2(0p_{3/2})^4(0p_{1/2})^2(0d_{5/2})^3$
^{18}C	0^+	$(0s_{1/2})^2(0p_{3/2})^4(0p_{1/2})^2(0d_{5/2})^4$
^{19}C	$(\frac{1}{2}^+)$	$(0s_{1/2})^2(0p_{3/2})^4(0p_{1/2})^2(0d_{5/2})^4(1s_{1/2})^1$
^{20}C	0^+	$(0s_{1/2})^2(0p_{3/2})^4(0p_{1/2})^2(0d_{5/2})^6$

The intrinsic densities of the carbon isotopes are calculated from a phenomenological mean-field potential. We assume a Slater determinant for the ground-state wave function of the carbon isotope. Table II lists the neutron configurations assumed for the ground states of the carbon isotopes. Some remarks on the configurations are made below. Though we assume that the last two neutrons occupy the $0d_{5/2}$ orbit for ^{16}C, its ground state is known to contain $(1s_{1/2})^2$ and $(0d_{5/2})^2$ configurations nearly equally [3,4]. We later take into account this fact using the ^{14}C+n+n model [5]. We consider two configurations for ^{17}C, the $(0d_{5/2})^2(1s_{1/2})$ and $(0d_{5/2})^3$ configurations. We assume the ground-state spin of ^{19}C to be $\frac{1}{2}^+$ and put the last neutron in the $1s_{1/2}$ orbit, following its one-neutron halo structure. The protons are assumed to occupy the $0s_{1/2}$ and $0p_{3/2}$ orbits for all the carbon isotopes.

The single-particle orbits arranged according to Table II are generated from the following mean-field potential

$$U(r) = -V_0 f(r) + V_1 r_0^2 \boldsymbol{\ell}\cdot\boldsymbol{s}\frac{1}{r}\frac{d}{dr}f(r) + V_c(r)\frac{1-\tau_3}{2}, \tag{14}$$

with $f(r)=\{1+\exp[(r-R)/a]\}^{-1}$. The radius and diffuseness parameters are chosen as $R = r_0 A^{1/3}$ with $r_0 = 1.25$ fm and $a = 0.65$ fm. The spin-orbit strength is set to follow the standard value [40],

$$V_1 = 22 - 14\frac{N-Z}{A}\tau_3\ (\mathrm{MeV}), \tag{15}$$

whereas the strength V_0 of the central part for neutron or proton is chosen so as to set the binding energy of the last nucleon equal to its separation energy, respectively. The asymptotic form of the single-nucleon wave function is satisfied by this requirement, which is important for the cross-section calculation as the surface region determines the range of reaction probability. Table III lists the V_0 values for both neutron and proton. The Coulomb potential for the proton orbits is taken as

$$V_c(r) = \begin{cases} \dfrac{(Z-1)e^2}{R}\left[\dfrac{3}{2} - \dfrac{1}{2}\left(\dfrac{r}{R}\right)^2\right] & \text{for } r \leqslant R \\ \dfrac{(Z-1)e^2}{r} & \text{for } r > R. \end{cases} \tag{16}$$

For the sake of simplicity, the radius parameter R is assumed to be the same as that of the mean-field potential.

The c.m. motion has to be subtracted appropriately from the Slater determinant to generate the intrinsic densities. The neutron or proton intrinsic density is defined as

$$\rho(\boldsymbol{r}) = \langle\Psi_0|\sum_i \delta(\bar{\boldsymbol{r}}_i - \boldsymbol{X} - \boldsymbol{r})P_i|\Psi_0\rangle, \tag{17}$$

where $\bar{\boldsymbol{r}}_i$ is the single-particle coordinate, $\boldsymbol{X}$ is the c.m. coordinate, and P_i is a projector for neutron or proton. Denoting the Slater determinant by Ψ, we obtain the neutron

TABLE III. Potential parameters V_0 in MeV in the mean-field model and in the core+n model which is applied to the odd N isotope. Two sets are used for ^{14}C: the shallower potential reproduces the neutron separation energy, whereas the deeper one is more appropriate to reproduce the size of ^{14}C. Two sets for ^{17}C correspond to the two different configurations in Table II.

Nucleus	Mean field		Core+n neutron
	Neutron	Proton	
^{12}C	57.83	57.93	
^{13}C	41.99	58.42	46.41
^{14}C	45.84	61.60	
	53.56	61.60	
^{15}C	40.09	60.34	50.31
^{16}C	49.28	60.99	
^{17}C	40.81	60.72	44.52
	39.83	60.72	
^{18}C	46.29	63.33	
^{19}C	37.84	63.59	40.91
^{20}C	41.27	65.04	

or proton density which contains the effect of the c.m. motion as

$$\tilde{\rho}(\boldsymbol{r}) = \langle\Psi|\sum_i \delta(\bar{\boldsymbol{r}}_i - \boldsymbol{r})P_i|\Psi\rangle = \sum_{nljm}|\psi_{nljm}(\boldsymbol{r})|^2, \quad (18)$$

where the sum extends over the occupied neutron or proton orbits depending on P_i. When the orbit with a certain nlj is not fully occupied, the average over m is taken in the above summation, that is Σ_m indicates $\Omega_j/(2j+1)\sum_{m=-j}^{j}$ with Ω_j being the number of neutrons occupying the nlj orbit. If the Slater determinant is approximated as a product of the intrinsic wave function Ψ_0 and the c.m. part $\Psi_{\rm cm}(\boldsymbol{X})$,

$$\Psi = \Psi_0\Psi_{\rm cm}(\boldsymbol{X}), \quad (19)$$

where

$$\Psi_{\rm cm}(\boldsymbol{X}) = \left(\frac{2A\nu}{\pi}\right)^{3/4}\exp(-A\nu X^2) \quad (20)$$

with a suitable oscillator parameter ν, it is easy to show that

$$\int d\boldsymbol{r}e^{i\boldsymbol{k}\cdot\boldsymbol{r}}\rho(\boldsymbol{r}) = \exp\left(\frac{k^2}{8A\nu}\right)\int d\boldsymbol{r}e^{i\boldsymbol{k}\cdot\boldsymbol{r}}\tilde{\rho}(\boldsymbol{r}). \quad (21)$$

Because the Fourier transform of $\tilde{\rho}$ is easily obtained, the above formula enables us to calculate the intrinsic density ρ through an inverse Fourier transformation of the right-hand side of Eq. (21).

The separability of Eq. (19) is in general not valid but holds exactly for such a case that the Slater determinant is built from the lowest configuration of the harmonic-oscillator shell model. We test the validity of separability by calculating the following overlap

$$o(\nu) = \frac{1}{A}\sum_{nljm}\left|\left\langle\psi^{\rm HO}_{nljm}(\nu)\right|\psi_{nljm}\right\rangle\right|^2, \quad (22)$$

where $\psi^{\rm HO}_{nljm}(\nu)$ is the harmonic-oscillator single-particle wave function with the oscillator parameter ν, and the sum of $nljm$ is taken over both the occupied neutron and proton orbits. We search for such ν that maximizes $o(\nu)$. The values of ν and $o(\nu)$ determined in this way are listed in Table IV. We find that $o(\nu)$ is close to unity, larger than 0.98 for even N isotopes, so that the intrinsic density may be calculated with use of Eq. (21). The $o(\nu)$ value for odd N nuclei decreases to about 0.95. The separability for this case is not as good as for even N case, but the separability assumption may still be acceptable.

Figure 3(a) displays the root-mean-square (rms) radii of neutron, proton and matter distributions assuming a pointlike nucleon. Corresponding to the large proton separation energies of the carbon isotopes, the proton radii remain nearly constant in the range of 2.3–2.4 fm. Assuming the charge radius of the proton to be 0.85 fm, we find that the charge radii of ^{12,13,14}C are 2.48, 2.47, and 2.46 fm, respectively, which are compared to the experimental values [41], 2.4715, 2.4795, and 2.4962 fm. The agreement with experiment is very good.

In contrast to the proton radius, the neutron radii change drastically reflecting the even-oddness of the neutron number. The isotope with odd N has much smaller neutron separation energy than the isotope with $N-1$. Consequently the value of V_0 becomes small and all the occupied neutron orbits tend to extend to larger distances, resulting in a considerable increase of the rms radius. See Fig. 4 later. As the reaction cross section for an odd N nucleus will turn out to be too large, we will discuss its density beyond the mean-field approach.

TABLE IV. Criterion on the separability of the c.m. motion from the Slater determinant wave functions. ν is the parameter of the harmonic-oscillator potential well. See Table III for the two sets of ^{14}C and ^{17}C.

Nucleus	$(2\nu)^{-1/2}$ (fm)	$o(\nu)$
^{12}C	1.61	0.998
^{13}C	1.72	0.988
^{14}C	1.69	0.992
	1.64	0.996
^{15}C	1.79	0.944
^{16}C	1.71	0.992
^{17}C	1.82	0.958
	1.82	0.973
^{18}C	1.75	0.988
^{19}C	1.89	0.949
^{20}C	1.83	0.980

Another point to be noted in Fig. 3(a) is that the neutron radius of ^{14}C given by the present model is much larger than that of ^{12}C. This is in contrast to the result of Ref. [10], in which the radii of both nuclei remain almost the same. In fact, we will see later that the reaction cross section for ^{14}C+^{12}C is too large to be compared to experiment. Thus the present mean-field description does not seem to work well for ^{14}C, and the molecular model [9] or ^{12}C+n+n three-body model may be promising in producing its better density. Related to the radius problem of ^{14}C, we note that the V_0 value for ^{14}C strongly deviates from the systematics of the potential strength for even N nucleus. According to Ref. [40], the potential strength for a neutron is

$$V_0 = 51 - 33\frac{N-Z}{A}\ (\text{MeV}). \quad (23)$$

Compared to this value, the V_0 value listed in the table is deeper by about 6 MeV for even N nuclei, but it is nearly equal for ^{14}C. We test a deeper value of V_0 for ^{14}C as listed in Table III. This parameter set turns out to be more suitable for ^{14}C, so it will be used to generate the densities of ^{15}C and ^{16}C in the dynamical model, which will be discussed in the next section.

IV. DENSITY WITH A DYNAMICAL MODEL

In the previous section, the neutron (proton) separation energy was used to determine all of the occupied single-particle orbits. For the nucleus with odd N, the neutron separation energy is small, so all the neutrons result in moving in a shallow potential well. Because of this, the radii of the odd N isotopes tend to be too large. To improve this restricted description, one has to go beyond a Slater determinant model by allowing for

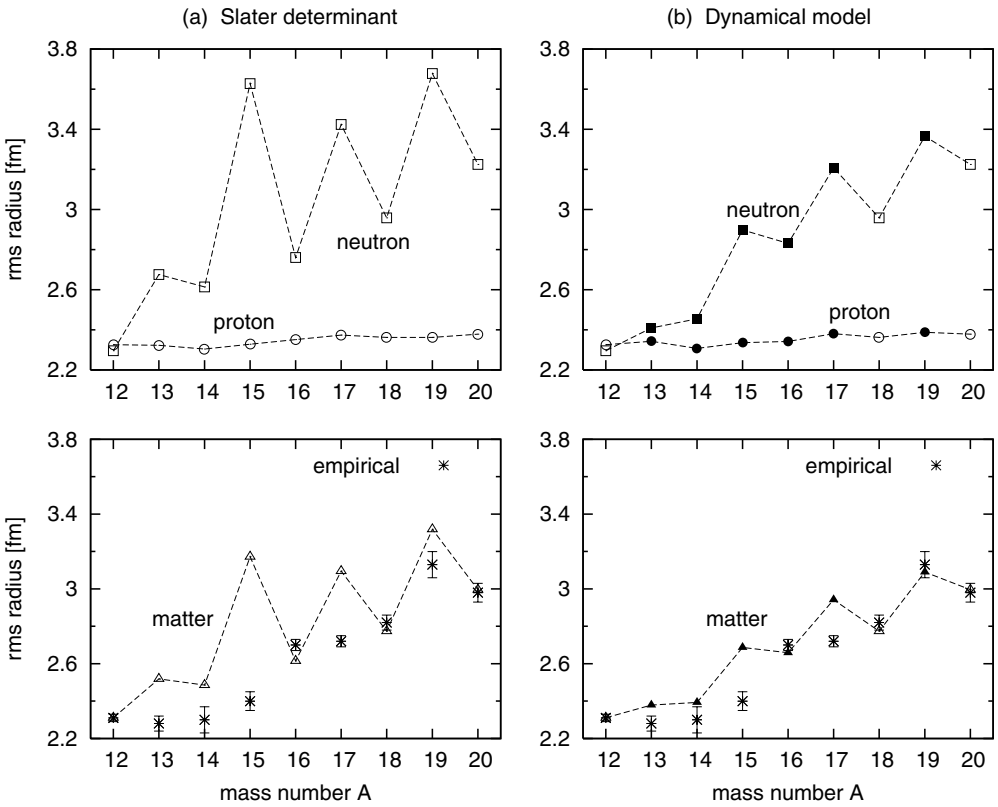

FIG. 3. Neutron, proton and matter radii of the carbon isotopes. The results with the Slater determinants are shown in panel (a), whereas those improved with the core+n and core+n+n models are shown in panel (b). See the text for detail. The empirical matter radii are taken from Ref. [13].

the degree of freedom of "clustering." The isotope with odd N will be described with a core nucleus with the even number $(N-1)$ of neutrons and a neutron. Here the last neutron is required to have the experimental separation energy, whereas the core nucleus is described as its subsystem independently from the separation energy of the last neutron.

We also consider the partition of a particular system into a core nucleus plus two neutrons, e.g., a ^{14}C+n+n model for ^{16}C and a ^{20}C+n+n model for ^{22}C. The motivation for this model is as follows. The last two neutrons in ^{16}C are found to have nearly equal amount of $(1s_{1/2})^2$ and $(0d_{5/2})^2$ configurations [3,5]. It is thus impossible to approximate the ground state of ^{16}C with a single Slater determinant. As for ^{22}C, ^{21}C is unstable with respect to a neutron emission, and ^{22}C becomes a Borromean system as the partition of ^{20}C+n+n. Thus the core+n+n model appears more realistic for ^{22}C than the Slater determinant model. These core+n+n models have been worked out in Refs. [4,5,8].

A. Density in a core+n model

A core+n model is applied to the odd isotopes, ^{13,15,17,19}C, where the corresponding cores are ^{12,14,16,18}C, respectively. For ^{17}C, the last neutron is assumed to be in the $1s_{1/2}$ orbit. Let $\Psi_0 = \Phi_c \Phi_{1n}$ denote the intrinsic wave function of the core+n model, where Φ_c represents the intrinsic wave function of the core nucleus and Φ_{1n} the relative motion function between the neutron and the core nucleus. The core nucleus can be described in exactly the same way as in the previous section, whereas the motion of the last neutron for a specified quantum number is determined from the n-core potential taken as the form of Eq. (14) with $A(N)$ being replaced by $A-1(N-1)$, the mass (neutron) number of the core nucleus. The potential strength V_0 is set to reproduce the neutron separation energy, and it is listed in Table III.

The intrinsic proton density is given by

$$\rho^p(\boldsymbol{r}) = \langle \Phi_{1n}(\boldsymbol{\rho}) | \rho_c^p \left(\frac{1}{A}\boldsymbol{\rho} + \boldsymbol{r} \right) | \Phi_{1n}(\boldsymbol{\rho}) \rangle, \tag{24}$$

and similarly the neutron density is

$$\begin{aligned} \rho^n(\boldsymbol{r}) \;=\; & \langle \Phi_{1n}(\boldsymbol{\rho}) | \rho_c^n \left(\frac{1}{A}\boldsymbol{\rho} + \boldsymbol{r} \right) | \Phi_{1n}(\boldsymbol{\rho}) \rangle \\ & + \langle \Phi_{1n}(\boldsymbol{\rho}) | \delta \left(\frac{A-1}{A}\boldsymbol{\rho} - \boldsymbol{r} \right) | \Phi_{1n}(\boldsymbol{\rho}) \rangle. \end{aligned} \tag{25}$$

Here $\boldsymbol{\rho}$ is the distance vector from the c.m. of the core to the last neutron, and ρ_c is the intrinsic density of the core nucleus. The integration with respect to the spin coordinate of the neutron should be done though it is not explicitly written in these equations.

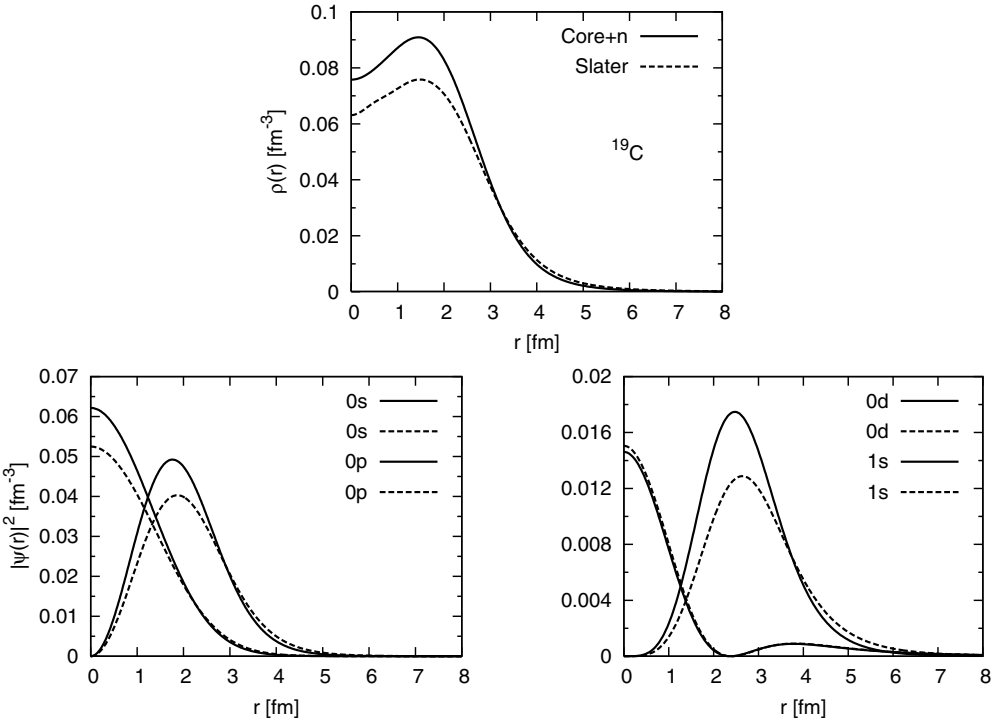

FIG. 4. Comparison of the neutron density of ^{19}C between the Slater determinant model and the dynamical model of ^{18}C+n. The lower panels show the decomposition of the density into the contributions of the neutron orbits with different orbital angular momenta. The c.m. motion is included.

We compare in Fig. 4 the neutron density of ^{19}C between the Slater determinant model and the dynamical ^{18}C+n model. The contribution of the neutron orbits to the density is also displayed in two lower panels for each orbital angular momentum to clarify the difference in the radial extension. The density of the Slater determinant model extends radially to further distances than that of the dynamical model. Particularly the $0p$ and $0d$ orbits play the most important role in producing the different neutron size.

The resulting radii calculated in the core+n model are displayed in Fig. 3(b) by closed square (for neutron), closed circle (for proton), and closed triangle (for matter), respectively. We see that the core+n model leads to a substantial reduction in the neutron radius, resulting in a fair improvement for the matter radius. The matter radius of ^{19}C especially is in good agreement with the empirical value. The matter radii of ^{15}C and ^{17}C are, however, still too large compared to the empirical ones.

B. ^{22}C in a ^{20}C+n+n model

The ground state of ^{22}C in the core+n+n model [8] is given by

$$\Psi = \Phi_{\rm c}\Phi_{2n}(\boldsymbol{x}_1, \boldsymbol{x}_2), \tag{26}$$

where the two-neutron wave function Φ_{2n} is expressed with the n-core relative coordinates, $\boldsymbol{x}_1$ and $\boldsymbol{x}_2$, again suppressing the spin coordinates. The valence neutron part Φ_{2n} is obtained in a combination of correlated Gaussian bases, $\Phi_{2n} = \Sigma_i C_i \Phi(\Lambda_i, A_i)$, with

$$\Phi(\Lambda, A) = (1 - P_{12}) \times \{e^{-\frac{1}{2}\tilde{\boldsymbol{x}}A\boldsymbol{x}}[[\mathcal{Y}_\ell(\boldsymbol{x}_1)\mathcal{Y}_\ell(\boldsymbol{x}_2)]_L \chi_S(1,2)]_{00}\}, \tag{27}$$

where P_{12} permutes the neutron coordinates and $\tilde{\boldsymbol{x}}A\boldsymbol{x} = A_{11}\boldsymbol{x}_1^2 + 2A_{12}\boldsymbol{x}_1 \cdot \boldsymbol{x}_2 + A_{22}\boldsymbol{x}_2^2$. The angular parts of the two-neutron motion are described using $\mathcal{Y}_{\ell m}(\boldsymbol{r}) = r^\ell Y_{\ell m}(\hat{\boldsymbol{r}})$ and they are coupled with the spin part χ_S to the total angular momentum zero. The basis function is specified by a set of angular momenta $\Lambda = (\ell, S)$ ($L = S$) and a 2×2 symmetric matrix A ($A_{21} = A_{12}$). The two neutrons are explicitly correlated due to the term $A_{12}\boldsymbol{x}_1\cdot\boldsymbol{x}_2$, the inclusion of which assures a precise solution in a relatively small dimension [42].

The two-neutron wave function Φ_{2n} is determined by solving the relevant three-body problem of the Hamiltonian

$$H = T_{\boldsymbol{\lambda}} + T_{\boldsymbol{\rho}} + U_1 + U_2 + v_{12} \tag{28}$$

under the Pauli constraint that Φ_{2n} should be orthogonal to any orbits occupied in the core nucleus ^{20}C. The subscripts, $\boldsymbol{\lambda}$ and $\boldsymbol{\rho}$, of the kinetic energies stand for the relative distance vectors of the three-body system: $\boldsymbol{\lambda} = \boldsymbol{x}_1 - \boldsymbol{x}_2$ and $\boldsymbol{\rho} = \frac{1}{2}(\boldsymbol{x}_1 + \boldsymbol{x}_2)$. The two-neutron potential v_{12} is taken from the realistic G3RS (case 1) potential [43] that contains central, tensor, and spin-orbit forces and reproduces the nucleon-nucleon scattering data as well as the deuteron properties. The n-^{20}C potential U_i is taken in the form of Eq. (14) augmented with an additional

term:

$$U = -V_0 f(r) + V_1 r_0^2 \boldsymbol{\ell}\cdot\boldsymbol{s}\frac{1}{r}\frac{d}{dr}f(r) + V_s e^{-\mu r^2}\mathcal{P}_s. \quad (29)$$

The operator $\mathcal{P}_s$ of the last term projects to the s wave of the n-^{20}C relative motion, so this term modifies the s-wave potential strength. In evaluating angular-momentum-dependent matrix elements in the basis of Eq. (27), we have neglected a small difference between the $\boldsymbol{x}_1, \boldsymbol{x}_2$ coordinate and the Jacobi coordinate as the core mass is much larger than the neutron mass. To determine the parameters of U, we take into account the conditions that (i) the $1s_{1/2}$ orbit is unbound as ^{21}C is unstable for a neutron emission and (ii) the $0d_{5/2}$ orbit is bound by at most 2.93 MeV, which is the neutron separation energy of ^{20}C. Because no information is available to determine the s-wave strength except that the $1s_{1/2}$ orbit is unbound, we vary V_s in a reasonable range. The range parameter μ is set to be $\mu = 0.09\,\mathrm{fm}^{-2}$. The value of V_0 is 43.24 MeV (set B of Ref. [8]) and V_1 is fixed to be 25.63 MeV ($N = 14$, $Z = 6$ in Eq. (15)).

Table V lists the ground-state energy E of ^{22}C with respect to the ^{20}C$+n+n$ threshold together with the rms neutron, proton and matter radii for some values of V_s. The calculated energies are all within the uncertainty of the experimental value (-0.423 ± 1.140 MeV). If one chooses a smaller value than 9.46 MeV for V_s, the $1s_{1/2}$ orbit would be bound. We see from the table that the neutron radius increases considerably as the s wave potential strength decreases. A slight change of the proton radius is due to the change of the two-neutron wave function, as will be discussed in the next subsection.

C. Density in a core+n+n model

The intrinsic neutron density for the core$+n+n$ system is obtained by

$$\rho^n(\boldsymbol{r}) = \langle\Phi_{2n}(\boldsymbol{x}_1,\boldsymbol{x}_2)|\rho_c^n\left(\frac{2}{A}\boldsymbol{\rho}+\boldsymbol{r}\right)|\Phi_{2n}(\boldsymbol{x}_1,\boldsymbol{x}_2)\rangle + \rho_{2n}(\boldsymbol{r}), \quad (30)$$

where

$$\rho_{2n}(\boldsymbol{r}) = \langle\Phi_{2n}(\boldsymbol{x}_1,\boldsymbol{x}_2)|\sum_{i=1}^{2}\delta\left(\boldsymbol{x}_i - \frac{2}{A}\boldsymbol{\rho} - \boldsymbol{r}\right)|\Phi_{2n}(\boldsymbol{x}_1,\boldsymbol{x}_2)\rangle \quad (31)$$

TABLE V. Properties of ^{22}C for different V_s values of the n-^{20}C potential. E is the ground-state energy in MeV with respect to the ^{20}C$+n+n$ threshold, and $\langle r_n^2\rangle^{1/2}$, $\langle r_p^2\rangle^{1/2}$, and $\langle r_m^2\rangle^{1/2}$ denote the rms neutron, proton, and matter radii given in fm, respectively.

V_s	E	$\langle r_n^2\rangle^{1/2}$	$\langle r_p^2\rangle^{1/2}$	$\langle r_m^2\rangle^{1/2}$
9.46	−0.489	3.96	2.43	3.61
9.90	−0.361	4.07	2.44	3.69
10.4	−0.232	4.24	2.45	3.83
10.9	−0.122	4.58	2.48	4.11

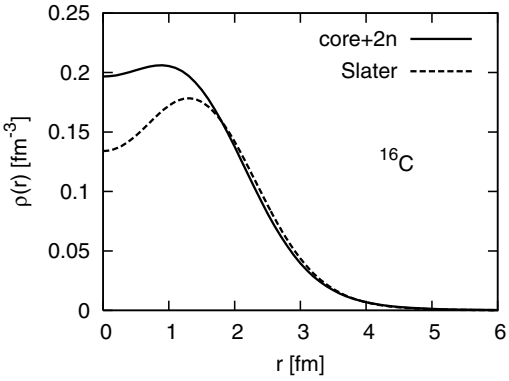

FIG. 5. Comparison of the matter density of ^{16}C between the Slater determinant model and the ^{14}C$+n+n$ model.

is the contribution of the two neutrons to the neutron density. The intrinsic proton density is given by

$$\rho^p(\boldsymbol{r}) = \langle\Phi_{2n}(\boldsymbol{x}_1,\boldsymbol{x}_2)|\rho_c^p\left(\frac{2}{A}\boldsymbol{\rho}+\boldsymbol{r}\right)|\Phi_{2n}(\boldsymbol{x}_1,\boldsymbol{x}_2)\rangle. \quad (32)$$

We use the intrinsic core density obtained in Sec. III. A method of calculation for the density with the correlated Gaussians $\Phi_{2n}(\boldsymbol{x}_1,\boldsymbol{x}_2)$ is given in Appendix.

We compare in Fig. 5 the densities for ^{16}C obtained with the Slater determinant and the dynamical core$+n+n$ model. The dynamical model with ^{14}C$+n+n$ allows us to include both of the d and s waves for the last neutrons. This is the reason why the central density rises compared to that with the Slater determinant where the last two neutrons are restricted to the $(0d_{5/2})^2$ configuration. It is also noted that the density of the dynamical model is larger at large distances ($r \geqslant 4.0$ fm) than that of the Slater determinant model. As shown in Fig. 3(b), the matter radius of ^{16}C calculated in the dynamical model slightly increases compared to that of the Slater determinant model, and it is in good agreement with the empirical value.

Figure 6 displays the two-neutron density distribution $\rho_{2n}(\boldsymbol{r})$ of ^{22}C for the potential parameters given in Table V. The density decreases slowly for increasing r, reaching far distances. The two-neutron density is found to dominate the total neutron density of ^{22}C for $r > 6$ fm [8]. The position of the dip hardly alters against the change of V_s, which is because

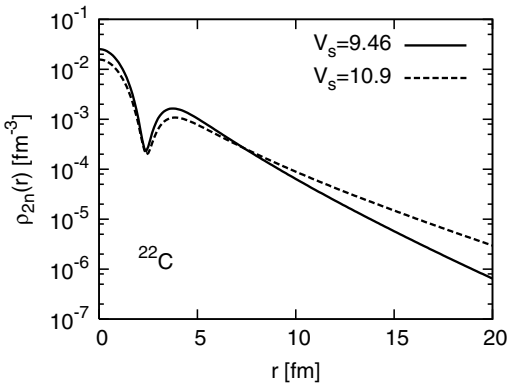

FIG. 6. The two-neutron densities of ^{22}C for some of the potential parameters of Table V.

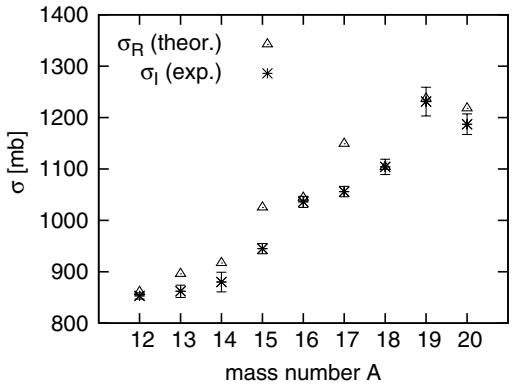

FIG. 7. The reaction cross sections of the carbon isotopes on a ^{12}C target calculated with the NTG model. The experimental data cited here are the interaction cross sections [13]. The incident energy of the projectile nucleus is around 950A MeV, except for ^{15}C performed at 740A MeV.

the dip appears as a consequence of the Pauli orthogonality constraint to the orbits occupied in the core mentioned above.

V. NUMERICAL RESULTS

In this section, we show our numerical results of the total reaction cross sections of the carbon isotopes on ^{12}C.

A. Reaction cross sections for ^{12}C to ^{20}C

The calculation of reaction cross section has been performed using the phase shift functions defined by Eqs. (4) (OLA), (8) (NTG), and (5) together with Eq. (12) (NTO). The densities used in the reaction calculation give the nucleon radii shown in Fig. 3(b). These densities are fitted in terms of a combination of Gaussians with different width parameters to facilitate the phase-shift calculation.

In Fig. 7, we plot the numerical results of NTG calculation of the reaction cross sections of the carbon isotopes on ^{12}C at high incident energy around 950A MeV. For comparison, we plot the data in the same figure. To compare the numerical results with experiment, we have to bear in mind that most of the cross sections measured at high energy are not reaction cross sections but interaction cross sections. The interaction cross section does not include the contribution from those inelastic processes that correspond to the excitation of the projectile to particle-bound excited states, so the interaction cross section is in general smaller than the total reaction cross section if such excited states exist. Actually, as was pointed out recently [44], there exists some difference between the total reaction cross section and the interaction cross section, about 80 mb, for the case of ^{12}C+^{12}C reaction. Because such difference depends on the nuclear structure, and no such data are available, we consider the difference as a kind of maximum uncertainty of our numerical results in this figure.

A comparison with experiment indicates that the numerical results of the reaction cross sections for ^{12,16,18,19,20}C agree with the interaction cross-section data, whereas those for ^{15,17}C are too large.

Whether the reaction cross section calculated for ^{14}C is quite reasonable or a little too large compared to experiment is not clear, because it is difficult to estimate possible contribution from the inelastic processes. For all the carbon isotopes with even N (except for ^{14}C), we have the densities which reproduce the experimental cross sections. We used these densities in the core+n description for the carbon isotopes with odd N. The reaction cross sections calculated with this model is found to bring a significant improvement in the agreement with experiment. Particularly, the agreement attained in ^{19}C is excellent, considering that the reaction cross section is equal to the interaction cross section for ^{19}C to good accuracy. For the case of ^{13}C, it is not clear whether the differences between theory and experiment can entirely be explained by the difference between the reaction cross section and the interaction cross section.

The reaction cross section for ^{16}C is calculated in the ^{14}C+n+n model using the improved density of ^{14}C. The two neutrons are restricted to neither $(1s_{1/2})^2$ nor $(0d_{5/2})^2$ configuration, but contains both of them together with other configurations [5]. We see that the calculated cross section turns out to be in almost perfect agreement with experiment within its error.

We predict in Fig. 8 the reaction cross sections of the carbon isotopes $^{13-20}$C on a ^{12}C target as a function of the incident energy. The reaction cross section predicted by the OLA is typically 50 mb larger than that predicted by the NTG except for the incident energy range of 80–150A MeV. This tendency is already seen in the ^{12}C+^{12}C case, as shown in Fig. 2. The energy dependence of both NTG and NTO cross sections is similar to that of the ^{12}C+^{12}C case displayed in Fig. 2. Very limited experimental data available at lower energies hamper a clear-cut conclusion. It appears, however, that the cases for ^{13,14,16}C are successfully reproduced. In contrast to these nuclei, the cross section of ^{15}C clearly indicates a marked discrepancy between theory and experiment: The theory underestimates the cross section at lower energy, but appears to overestimate it at high energy.

One might think that the above discrepancy in ^{15}C could be resolved by including its breakup effect into ^{14}C+n continuum states in the few-body (FB) framework of a core+n model [15,45,46]. This is not the case, however, because the NTO already takes into account most of the effect. In fact, we have compared the reaction cross sections between NTO and FB at several incident energies, and found that the difference between them is small even at low energy: For example, at the incident energy of 40A MeV, the σ_R value of ^{15}C+^{12}C is 1519 mb for NTO and 1525 mb for FB, whereas it is only 1425 mb for the folding model which uses Eq. (13) to obtain the phase shift function. Thus the increase of the reaction cross section given by FB compared to NTO is just 6 mb for ^{15}C, and 18 mb for ^{19}C. At the higher energy of 800A MeV, the FB cross section becomes only slightly smaller than the NTO cross section. The discrepancy observed in the reaction cross section of ^{15}C+^{12}C remains an open question.

B. Reaction cross section for ^{22}C

We display in Fig. 9 our prediction of the reaction cross section of ^{22}C+^{12}C as a function of the incident energy. As the reaction cross section increases for the increasing radius of the projectile and no information on the mass of ^{22}C is available,

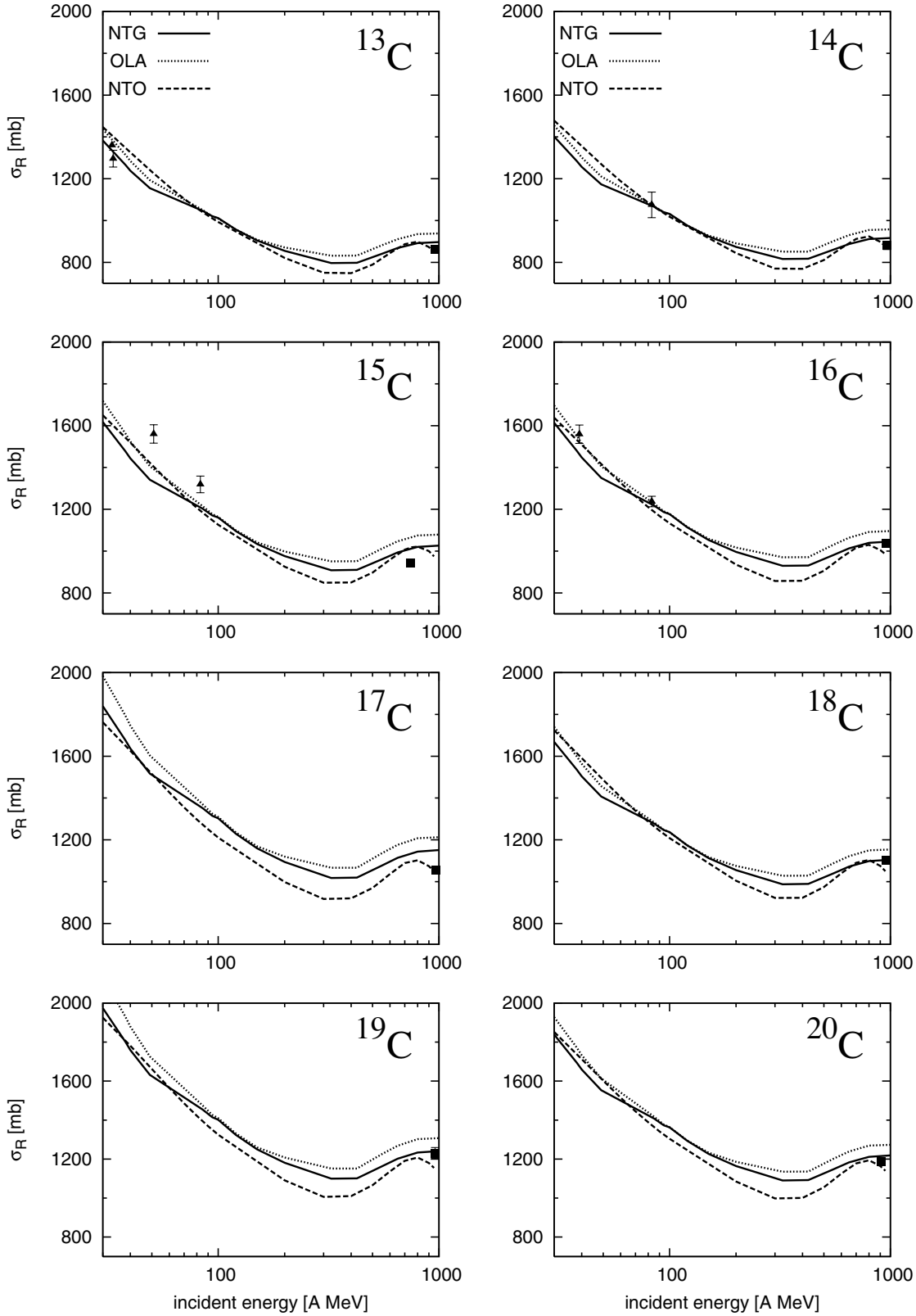

FIG. 8. Reaction cross sections for the collisions of the carbon isotopes on a ^{12}C target calculated with the NTG, NTO, and OLA models. The experimental data marked with the closed triangle and the closed square denote the reaction cross section and the interaction cross section [13], respectively. The reaction cross-section data are taken from Refs. [27,47] for ^{13}C, from Ref. [48] for ^{14,15}C, and from Refs. [27,29] for ^{16}C.

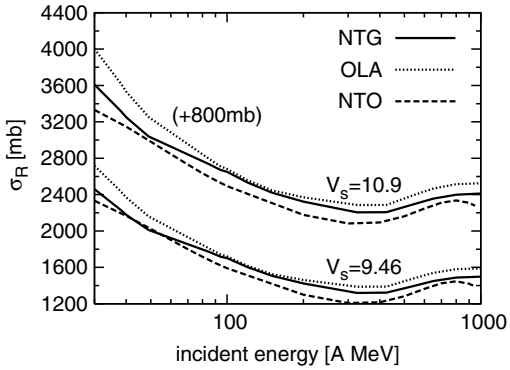

FIG. 9. Prediction of the reaction cross section for the collision of ^{22}C on a ^{12}C target as a function of the incident energy. See Table V for the two values of V_s.

we plot two cases obtained using the densities that correspond to the two extremes in Table V, namely $V_s = 9.46$ and 10.9 MeV. The matter radius obtained with the latter parameter is larger by 11% than that with the former parameter.

The cross sections calculated with the NTG and NTO models are in reasonable agreement, whereas the OLA cross section at lower energy shows an enhancement of about 10% compared to the NTG cross section. According to the NTG calculation, the total reaction cross section of ^{22}C is estimated to be 2200–2450 mb at 40A MeV and 1500–1600 mb around 900A MeV.

To see the implication of these results, we refer to the black-sphere picture [49,50] or the strong absorption model [16]: These pictures include only one scale, the nuclear radius, a. If one determine the values of a so as to reproduce the angle of the first diffraction maximum in the proton-nucleus elastic-scattering data, the absorption cross section, πa^2, agrees with the empirical total reaction cross section [50]. This a can be regarded as a "reaction radius," inside which the reaction with incident protons occurs.

Because the data of p+^{22}C elastic differential cross section are not available, we may estimate the reaction radius through

$$\sigma_{\mathrm{R}}(P+T) = \pi(R_P + R_T)^2, \tag{33}$$

where R_P and R_T are the reaction radii of the projectile and target, respectively [50]. For a ^{12}C target we obtain $R_T = 2.69$ fm [50]. The reaction radius of *stable* nuclei follows $1.21\,A^{1/3}$ fm. If we apply it to the above expression, we obtain 1170 mb, much smaller than the result around 900A MeV. This supports the much more extended matter distribution of ^{22}C than the stable nuclei of the same mass number.

Based on the above expression, the reaction radius of ^{22}C may be estimated by

$$R_{^{22}\mathrm{C}} = \left(\sqrt{\frac{4\sigma_{\mathrm{R}}(^{22}\mathrm{C}+^{12}\mathrm{C})}{\sigma_{\mathrm{R}}(^{12}\mathrm{C}+^{12}\mathrm{C})}} - 1\right) R_{^{12}\mathrm{C}}. \tag{34}$$

Using the reaction cross sections calculated at high energy together with $R_{^{12}\mathrm{C}} = \sqrt{\sigma_{\mathrm{R}}(^{12}\mathrm{C}+^{12}\mathrm{C})/4\pi}$ leads to the estimation that the reaction radius of ^{22}C, $R_{^{22}\mathrm{C}}$, is about 4.41 fm. Multiplying it by $\sqrt{3/5}$, we obtain 3.41 fm for the rms reaction radius of ^{22}C, which is smaller than the rms matter radii listed in Table V. For lighter stable nuclei, typically $A < 50$, the rms reaction radii are usually smaller than the rms matter radii [50]. Because light nuclei have no sharp surface, the reaction occurs inside compared to heavier nuclei.

Actually, for the data of incident energies higher than $\sim$800A MeV, $\sqrt{3/5}a$ systematically deviates from the empirically deduced values of the rms matter radius for nuclei having mass number less than about 50, whereas it almost completely agrees with the deduced values for $A \gtrsim 50$. This tendency suggests a significant change of the nuclear matter distribution from a rectangular one for $A \lesssim 50$, which is consistent with the behavior of the empirical charge distribution. Therefore, the above result of ^{22}C suggests that such feature of light nuclei still persists in ^{22}C although it has a large radius comparable to much heavier nuclei.

Measurements of the reaction cross section as well as the mass of ^{22}C are indispensable for the determination of its radius.

VI. SUMMARY

We have systematically analyzed the total reaction cross sections of carbon isotopes with $N = 6$–16 on a ^{12}C target for wide range of incident energy from 40 to 1000A MeV.

The structure of the carbon isotopes has first been described by a Slater determinant generated from a phenomenological mean-field potential. The potential depth of Woods-Saxon type is determined separately for neutron and proton to reproduce the nucleon separation energy. The intrinsic density of each carbon isotope is built from the single-particle states by separating, in a good approximation, the center-of-mass motion from the Slater determinant. This model reasonably well describes the ground states of even N isotopes, but the mean-field potential for odd N isotope tends to be too shallow, yielding too large neutron and matter radii. This unrealistic feature has been largely improved by performing separate studies which take into account their specific structure of core+n. We have also performed the core+n+n three-body model for ^{16}C and ^{22}C, to take into account the mixing of the sd orbits in ^{16}C and a Borromean character of ^{22}C, respectively.

For calculations of the cross sections, we take two schemes: one is the Glauber approximation, and the other is the eikonal model using a global optical potential. It is vital to find a consistent parametrization of the nucleon-nucleon scattering amplitude in the former model. The parameters we find for the NN profile function are different from previous ones, and they have successfully reproduced the data on ^{12}C+^{12}C reaction cross sections from 40 to 1000A MeV incident energies. The both reaction schemes reasonably well reproduce the data of the cross sections of ^{13}C, ^{14}C, and ^{16}C on ^{12}C that are available at low and high incident energies. Those data which are available for ^{18}C, ^{19}C, and ^{20}C around 950A MeV are all reproduced very well by the Glauber theory.

Compared to the empirical radii of the carbon isotopes tabulated in Ref. [13], our dynamical model gives too large values for ^{15}C (see Fig. 3(b)). From this comparison, we expect that the reaction cross section predicted by the present model is larger than the experiment. In fact, this is true for

the high-energy data at 740A MeV, but it is just opposite at low energy. See Fig. 8. It is an open question that the calculated reaction cross sections of ^{15}C, though our calculation practically includes the breakup effect, is found to underestimate the empirical values observed at low energy.

The radius of ^{17}C is also calculated to be too large. Even in the ^{16}C+n dynamical version, we do not consider that the model for ^{17}C is probably very realistic. More sophisticated structure model will be necessary.

We have predicted the total reaction cross section of ^{22}C on ^{12}C. In our model ^{22}C has extremely large size comparable to that of a medium heavy nucleus. Our prediction for the cross section is at variance with the binding energy of the two neutrons: According to the Glauber calculation, the reaction cross section of ^{22}C is 2200–2450 mb at 40A MeV and 1500–1600 mb around 900A MeV. Measurements of the reaction cross section as well as the mass of ^{22}C will be useful to determine the structure of ^{22}C.

Our framework offers a prescription for simple, consistent analyses of broad range of reaction cross-section data of neutron-rich unstable nuclei. Such data are expected to be provided by radioactive ion beam facilities, such as GSI and Radioactive Ion Beam Factory at RIKEN.

ACKNOWLEDGMENTS

We acknowledge T. Motobayashi for his encouragement during the course of this work. We also acknowledge M. Takechi and M. Fukuda for providing us with data on ^{12}C+^{12}C reaction cross sections. A.K. thanks K. Iida, K. Oyamatsu, and M. Takashina for useful comments and helpful discussions. This work was in part supported by a Grant for Promotion of Niigata University Research Projects (2005–2007).

APPENDIX: CALCULATION OF A TWO-PARTICLE DISTRIBUTION FUNCTION

The aim of this appendix is to outline a method of calculation for the density which appears in Sec. IV C. Expressing the core density in Eqs. (30) and (32) as

$$\rho_{\rm c}\left(\frac{2}{A}\boldsymbol{\rho}\right) = \int \delta\left(\frac{2}{A}\boldsymbol{\rho} - \boldsymbol{r}\right)\rho_{\rm c}(\boldsymbol{r})d\boldsymbol{r} \tag{A1}$$

with $\boldsymbol{\rho} = \frac{1}{2}(\boldsymbol{x}_1 + \boldsymbol{x}_2)$, we note that the terms in Eqs. (30), (31), and (32) are all reduced to the calculation of the two-particle distribution function

$$\begin{aligned} D(w,\boldsymbol{r}) &= \langle [G_S(A',\ell')\chi_S(1,2)]_{00}| \\ &\quad \times \delta(\tilde{w}\boldsymbol{x} - \boldsymbol{r})|[G_S(A,\ell)\chi_S(1,2)]_{00}\rangle. \end{aligned} \tag{A2}$$

Here the function G is a short-hand notation for

$$G_{LM}(A,\ell) = {\rm e}^{-\frac{1}{2}\tilde{\boldsymbol{x}}A\boldsymbol{x}}[\mathcal{Y}_\ell(\boldsymbol{x}_1)\mathcal{Y}_\ell(\boldsymbol{x}_2)]_{LM}, \tag{A3}$$

and $\tilde{w}\boldsymbol{x}$ stands for $w_1\boldsymbol{x}_1 + w_2\boldsymbol{x}_2$, where w_1 and w_2 are constants that are chosen appropriately depending on the two-particle distribution function to be evaluated. A choice of $w_1 = 1 - \frac{1}{A}$ and $w_2 = -\frac{1}{A}$ or $w_1 = -\frac{1}{A}$ and $w_2 = 1 - \frac{1}{A}$ is made for the evaluation of the density of Eq. (31), while $w_1 = w_2 = \frac{1}{A}$ is chosen for Eqs. (30) and (32).

After integrating over the spin coordinates, we obtain

$$\begin{aligned} D(w,\boldsymbol{r}) &= \sum_\lambda C_\lambda(\ell\ell' S)\iint {\rm e}^{-\frac{1}{2}\tilde{\boldsymbol{x}}B\boldsymbol{x}}(x_1x_2)^{\ell+\ell'} \\ &\quad \times [Y_\lambda(\widehat{\boldsymbol{x}_1})Y_\lambda(\widehat{\boldsymbol{x}_2})]_{00}\delta(\tilde{w}\boldsymbol{x} - \boldsymbol{r})d\boldsymbol{x}_1 d\boldsymbol{x}_2, \end{aligned} \tag{A4}$$

where $B = A + A'$ and

$$C_\lambda(\ell\ell' S) = \frac{(2\ell+1)(2\ell'+1)}{4\pi(2\lambda+1)\sqrt{2S+1}}\langle \ell 0\ell' 0|\lambda 0\rangle^2 U(\ell\lambda S\ell';\ell'\ell). \tag{A5}$$

Here U is a unitary Racah coefficient, and λ takes those values from $|\ell - \ell'|$ to $\ell + \ell'$ which satisfy the condition of $\lambda + \ell + \ell'$ = even.

The integration $\mathcal{I}$ in Eq. (A4) can be performed by a change of variables from $\boldsymbol{x}$ to $\boldsymbol{y}$, $\boldsymbol{x} = W\boldsymbol{y}$, under the condition that $\boldsymbol{y}_2$ is set equal to $\tilde{w}\boldsymbol{x}$. Though $\boldsymbol{y}_1$ can be chosen arbitrarily as long as it is independent of $\boldsymbol{y}_2$, we here choose W as follows:

$$W = \frac{1}{w_1^2 + w_2^2}\begin{pmatrix} w_2 & w_1 \\ -w_1 & w_2 \end{pmatrix}. \tag{A6}$$

Substituting $\boldsymbol{x} = W\boldsymbol{y}$ in Eq. (A4) and noting that $[Y_\lambda(\widehat{\boldsymbol{x}_1})Y_\lambda(\widehat{\boldsymbol{x}_2})]_{00}$ can be expressed in terms of a Legendre polynomial $P_\lambda(\zeta)$ with $\zeta = (\boldsymbol{x}_1\cdot\boldsymbol{x}_2)/(x_1x_2)$, we obtain

$$\mathcal{I} = (\det W)^3 \iint {\rm e}^{-\frac{1}{2}\tilde{\boldsymbol{y}}\bar{B}\boldsymbol{y}}F_1(\boldsymbol{y})F_2(\boldsymbol{y})\delta(\boldsymbol{y}_2 - \boldsymbol{r})d\boldsymbol{y}_1 d\boldsymbol{y}_2, \tag{A7}$$

where $\bar{B} = \tilde{W}BW$ and

$$\begin{aligned} F_1(\boldsymbol{y}) &= (x_1x_2)^{\ell+\ell'-\lambda} = (\det W)^{2(\ell+\ell'-\lambda)}\{|w_2\boldsymbol{y}_1 + w_1\boldsymbol{y}_2| \\ &\quad \times |-w_1\boldsymbol{y}_1 + w_2\boldsymbol{y}_2|\}^{\ell+\ell'-\lambda}, \end{aligned} \tag{A8}$$

and

$$\begin{aligned} F_2(\boldsymbol{y}) &= (x_1x_2)^\lambda[Y_\lambda(\widehat{\boldsymbol{x}_1})Y_\lambda(\widehat{\boldsymbol{x}_2})]_{00} \\ &= \frac{(-1)^\lambda\sqrt{2\lambda+1}}{4\pi}(\det W)^{2\lambda} \\ &\quad \times \sum_{k=0}^{[\frac{\lambda}{2}]}(-1)^k\frac{(2\lambda-2k-1)!!}{(\lambda-2k)!(2k)!!} \\ &\quad \times \{(w_2\boldsymbol{y}_1 + w_1\boldsymbol{y}_2)\cdot(-w_1\boldsymbol{y}_1 + w_2\boldsymbol{y}_2)\}^{\lambda-2k} \\ &\quad \times \{|w_2\boldsymbol{y}_1 + w_1\boldsymbol{y}_2|\,|-w_1\boldsymbol{y}_1 + w_2\boldsymbol{y}_2|\}^{2k}. \end{aligned} \tag{A9}$$

Both $F_1(\boldsymbol{y})$ and $F_2(\boldsymbol{y})$ are polynomials of y_1^2, y_2^2 and $\boldsymbol{y}_1\cdot\boldsymbol{y}_2$ as $\ell + \ell' - \lambda$ is an even integer, so that, with $\boldsymbol{y}_2$ being replaced by $\boldsymbol{r}$, $\mathcal{I}$ is reduced to the following type of elementary integrals

$$\int {\rm e}^{-py_1^2 + q\boldsymbol{r}\cdot\boldsymbol{y}_1}y_1^{2m}(\boldsymbol{r}\cdot\boldsymbol{y}_1)^n d\boldsymbol{y}_1, \tag{A10}$$

where both m and n are non-negative integers.

[1] N. Imai *et al*., Phys. Rev. Lett. **92**, 062501 (2004).
[2] Z. Elekes *et al*., Phys. Lett. **B586**, 34 (2004).
[3] T. Yamaguchi, T. Zheng, A. Ozawa, M. Chiba, R. Kanungo *et al*., Nucl. Phys. **A724**, 3 (2003).
[4] Y. Suzuki, H. Matsumura, and B. Abu-Ibrahim, Phys. Rev. C **70**, 051302(R) (2004).
[5] W. Horiuchi and Y. Suzuki, Phys. Rev. C **73**, 037304 (2006) [Erratum-*ibid*. **74**, 019901(E) (2006)].
[6] T. Nakamura *et al*., Phys. Rev. Lett. **83**, 1112 (1999).
[7] V. Maddalena *et al*., Phys. Rev. C **63**, 024613 (2001).
[8] W. Horiuchi and Y. Suzuki, Phys. Rev. C **74**, 034311 (2006).
[9] N. Itagaki, T. Otsuka, K. Ikeda, and S. Okabe, Phys. Rev. Lett. **92**, 142501 (2004).
[10] Y. Kanada-En'yo, Phys. Rev. C **71**, 014310 (2005).
[11] H. Sagawa, X. R. Zhou, X. Z. Zhang, and T. Suzuki, Phys. Rev. C **70**, 054316 (2004).
[12] B. A. Brown, Prog. Part. Nucl. Phys. **47**, 517 (2001); B.A. Brown, S. Typel, and W. A. Richter, Phys. Rev. C **65**, 014612 (2002).
[13] A. Ozawa, T. Suzuki, and I. Tanihata, Nucl. Phys. **A693**, 32 (2001).
[14] R. J. Glauber, in *Lectures in Theoretical Physics* (Interscience, New York, 1959), Vol. 1, p. 315.
[15] K. Yabana, Y. Ogawa, and Y. Suzuki, Nucl. Phys. **A539**, 295 (1992).
[16] Y. Suzuki, R. G. Lovas, K. Yabana, and K. Varga, *Structure and Reactions of Light Exotic Nuclei* (Taylor & Francis, London, 2003).
[17] K. Tanaka *et al*. (private communication).
[18] V. Franco and G. K. Varma, Phys. Rev. C **15**, 1375 (1977).
[19] K. Varga, S. C. Pieper, Y. Suzuki, and R. B. Wiringa, Phys. Rev. C **66**, 034611 (2002).
[20] B. Abu-Ibrahim and Y. Suzuki, Phys. Rev. C **61**, 051601(R) (2000).
[21] B. Abu-Ibrahim and Y. Suzuki, Phys. Rev. C **62**, 034608 (2000).
[22] S. M. Lenzi, A. Vitturi, and F. Zardi, Phys. Rev. C **40**, 2114 (1989).
[23] L. Ray, Phys. Rev. C **20**, 1857 (1979).
[24] M. Takechi, M. Fukuda, M. Mihara, T. Chinda, T. Matsumasa *et al*., Eur. Phys. J. A **25**, s01, 217 (2005); private communication.
[25] C. Perrin, S. Kox, N. Longequeue, J. B. Viano, M. Buenerd *et al*., Phys. Rev. Lett. **49**, 1905 (1982).
[26] H. Y. Zhang, W. Q. Shen, Z. Z. Ren, Y. G. Ma, W. Z. Jiang *et al*., Nucl. Phys. **A707**, 303 (2002).
[27] D. Q. Fang, W. Q. Shen, J. Feng, X. Z. Cai, J. S. Wang *et al*., Phys. Rev. C **61**, 064311 (2000).
[28] S. Kox, A. Gamp, C. Perrin, J. Arvieux, R. Bertholet *et al*., Phys. Rev. C **35**, 1678 (1987).
[29] T. Zheng, T. Yamaguchi, A. Ozawa, M. Chiba, R. Kanungo *et al*., Nucl. Phys. **A709**, 103 (2002).
[30] J. Y. Hostachy, M. Buenerd, J. Chauvin, D. Lebrun, Ph. Martin *et al*., Nucl. Phys. **A490**, 441 (1988).
[31] J. Jaros, A. Wagner, L. Anderson, O. Chamberlain, R. Z. Fuzesy *et al*., Phys. Rev. C **18**, 2273 (1978).
[32] N. J. Di Giacomo, J. C. Peng, and R. M. DeVries, Phys. Lett. **B101**, 383 (1981).
[33] R. E. Warner, I. J. Thompson, and J. A. Tostevin, Phys. Rev. C **65**, 044617 (2002).
[34] M. Fukuda (private communication).
[35] Y. Ogawa, K. Yabana, and Y. Suzuki, Nucl. Phys. **A543**, 722 (1992).
[36] Particle Data Group, Phys. Lett. **B592**, 1 (2004).
[37] E. D. Cooper, S. Hama, B. C. Clark, and R. L. Mercer, Phys. Rev. C **47**, 297 (1993).
[38] S. K. Charagi and S. K. Gupta, Phys. Rev. C **41**, 1610 (1990).
[39] K. Iida, A. Kohama, and K. Oyamatsu, arXiv:nucl-th/0601039; J. Phys. Soc. Japan (in press).
[40] A. Bohr and B. R. Mottelson, *Nuclear Structure* (Benjamin, New York, 1969), Vol. I.
[41] W. Ruckstuhl, B. Aas, W. Beer, I. Beltrami, K. Bos *et al*., Nucl. Phys. **A430**, 685 (1984).
[42] K. Varga and Y. Suzuki, Phys. Rev. C **52**, 2885 (1995); Y. Suzuki and K. Varga, *Stochastic Variational Approach to Quantum-Mechanical Few-Body Problems*, Lecture Notes in Physics (Springer, Berlin, 1998), Vol. m54.
[43] R. Tamagaki, Prog. Theor. Phys. **39**, 91 (1968).
[44] A. Kohama, K. Iida, and K. Oyamatsu (unpublished).
[45] J. S. Al-Khalili and J. A. Tostevin, Phys. Rev. Lett. **76**, 3903 (1996); J. S. Al-Khalili, J. A. Tostevin, and I. J. Thompson, Phys. Rev. C **54**, 1843 (1996).
[46] B. Abu-Ibrahim, Y. Ogawa, Y. Suzuki, and I. Tanihata, Comput. Phys. Commun. **151**, 369 (2003).
[47] M. Fukuda, T. Ichikawa, N. Inabe, T. Kubo, H. Kumagai *et al*., Phys. Lett. **B268**, 339 (1991).
[48] D. Q. Fang, T. Yamaguchi, T. Zheng, A. Ozawa, M. Chiba *et al*., Phys. Rev. C **69**, 034613 (2004).
[49] A. Kohama, K. Iida, and K. Oyamatsu, Phys. Rev. C **69**, 064316 (2004).
[50] A. Kohama, K. Iida, and K. Oyamatsu, Phys. Rev. C **72**, 024602 (2005).